Ocean Engineering 233 (2021) 109087

Contents lists available at ScienceDirect

Ocean Engineering

journal homepage: www.elsevier.com/locate/oceaneng

A numerical structural analysis of ducted, high-solidity, fibre-composite tidal turbine rotor configurations in real flow conditions

Mitchell G. Borg [a], Qing Xiao [a,*], Steven Allsop [b], Atilla Incecik [a], Christophe Peyrard [c]

[a] Department of Naval Architecture, Ocean, and Marine Engineering, University of Strathclyde, Glasgow, Scotland, United Kingdom
[b] Industrial Doctoral Centre for Offshore Renewable Energy (IDCORE), University of Edinburgh, Edinburgh, Scotland, United Kingdom
[c] Electricité de France Research and Development (EDF R&D), Chatou, Ile-de-France, France

ARTICLE INFO

Keywords:
Partitioned–approach
Fluid–structure interaction
High-solidity
Open-centre
Tidal turbine
Ducted turbine
Fibre-composite

ABSTRACT

Establishing a design and material evaluation of unique tidal turbine rotors in true hydrodynamic conditions by means of a numerical structural analysis has presented inadequacies in implementing spatial and temporal loading along the blade surfaces. This study puts forward a structural performance investigation of true-scale, ducted, high-solidity, fibre-composite tidal turbine rotor configurations in aligned and yawed flows by utilising outputs from unsteady blade-resolved computational fluid dynamic models as boundary condition loads within a finite-element numerical model. In implementation of the partitioned-approach fluid–structure interaction procedure, three distinct internal blade designs were analysed.

Investigating criteria related to structural deformation and induced strains, hydrostatic & hydrodynamic analyses are put forward in representation of the rotor within the flow conditions at the installation depth. The resultant axial deflections for the proposed designs describe a maximum deflection-to-bladespan ratio of 0.04, inducing a maximum strain of 0.9%. A fatigue response analysis is undertaken to acknowledge the blade material properties required to prevent temporal failure.

1. Introduction

Efforts to improve upon the efficacy of energy-generating turbines have been in constant development following system implementation in the global market. At the forefront of the pertinent research is the effort of increasing mass-flow through the rotor, along with the constrainment and alignment of the wake flow to facilitate further turbine installations (O Rourke et al., 2010). From the research attained, bi-directional ducts have been installed around a turbine rotor to enhance performance due to the acceleration of axial flow velocity through the duct throat as a result of the induced Venturi effect and pressure discrepancy (Kogan and Seginer, 1963; Borg et al., 2020, 2021).

Attributable to the potential augmentation in power extraction as a result of the increase in mass-flow, several commercial endeavours had attempted to adopt ducted turbine technology to achieve economic prospects. Amongst the ventures, DCNS/OpenHydro Ltd. had designed an open-centre ducted design approach (Bloomberg, 2020; OpenHydro Group Ltd., 2017). In open-water trials, a 2 MW turbine was successfully installed in the Bay of Fundy, Canada, portrayed in Fig. 1, together with a pair of 500 kW rated capacity turbines, as a demonstration array in Paimpol-Bréhat, Northern France, in collaboration with EDF France.

Albeit the enhancement in generated power, the structural response of a rotor within a bi-directional duct as a result of the flow acceleration under variant free-stream conditions is largely uncertain. Few research ventures have investigated the induced rotor mechanics in relation to the developed fluid dynamics, moreover upon the implementation of a duct feature in a turbine system, within aligned or misaligned flow (Nachtane et al., 2018; Allsop et al., 2018; Luquet et al., 2013; Boudounit et al., 2020). The analyses had put forward coupling approaches by extracting point-force loads or pressure distributions from empirical models, blade-element momentum theory (BEMT), or two-dimensional steady-state computational fluid dynamics as loading conditions within a structural model. Albeit applicable, the approaches do not account for time-dependent variations of induced static pressure and wall shear-stress due to distinct, three-dimensional, transient fluid dynamic phenomena, such as flow separation and turbulence effects. The implementation of a duct feature further magnifies the deficiencies as a result of the rotor being succumb to 'highly-loaded conditions', requiring validated three-dimensional high-fidelity fluid dynamic analyses in establishing the true load distribution.

* Corresponding author.
E-mail addresses: mitchell.borg@strath.ac.uk (M.G. Borg), qing.xiao@strath.ac.uk (Q. Xiao).

https://doi.org/10.1016/j.oceaneng.2021.109087
Received 26 March 2020; Received in revised form 1 March 2021; Accepted 7 April 2021
Available online 31 May 2021

Fig. 1. The 2 MW-rated OpenHydro ducted turbine.
Source: Adapted from The Canadian Press (2018), The Canadian Press/Andrew Vaughan, 2016.

In recognition of the loading variation upon power-generating operation, this study strived to overcome the related limitations by implementing a one-way computational fluid dynamic (CFD) and finite-element analysis (FEA) coupling with blade-explicit actuality to establish a partitioned-approach fluid–structure interaction (FSI) analysis. This permitted a structural evaluation in accordance to the modelled three-dimensional flow features, together with induced turbulence effects, at the rotor. Numerical validation of the computational fluid dynamic model was attained (Borg et al., 2020) in addition to the hydrodynamic outcomes of a full-scale, ducted turbine by comparing to literature (Betz, 1928) and blade-element momentum theory (Allsop et al., 2017). By utilising the numerical hydrodynamic outcomes, the aim of this research was to analyse the structural performance of three distinct rotor designs for a ducted, high-solidity tidal turbine when succumb to both aligned and yawed free-stream conditions. By means of this investigation, an appropriate rotor design was acknowledged, permitting a basis onto which optimisation of the blade structure parameters may be developed.

Literature has characterised evidence of rotor loading augmentation due to a shroud installation through several decades of research by means of analytical (Lilley and Rainbird, 1956), experimental (Kogan and Seginer, 1963), and numerical (Borg et al., 2020; Belloni et al., 2017; Allsop, 2018) analyses. Yet the conclusions have been put forward under the assumption of a rigid rotor structure. Amongst the fluid–structure numerically-coupled ducted tidal turbine structural investigations, Nachtane et al. (2018) utilised BEMT to predict the hydrodynamic performance of a bi-directional ducted tidal turbine in effort of establishing boundary conditions along the duct structure for a finite-element model. Similarly, Allsop et al. (2018) implemented BEMT outputs within a structural analysis code library designed to translate individual element forces into blade stresses. This was subsequently utilised to calculate the peak stress along the blades, as well as identifying stress concentration zones, to perform survivability assessments by incorporating non-uniform inflow profiles and blade weight forces to establish the degree of cyclic stresses under distinct operating conditions for a fatigue assessment. Additionally, Luquet et al. (2013) derived the pressure distribution along a ducted tidal turbine blade utilising CFD, noting that the outcome may be utilised within a finite-element analysis.

In distinction to ducted turbine analyses, a number of studies have established the fluid–structure coupling of bare turbines. The structural analyses were carried out for the purpose of material selection to distinguish between the utilisation of glass-fibre reinforced polymers (GFRPs) and carbon-fibre reinforced polymers (CFRPs) for blade spar caps and shear webs (Boudounit et al., 2020; Grogan et al., 2013; Leong et al., 2012) by considering the strains induced and flapwise deflection as properties for the material selection. The hydrodynamic loads had been established by means of BEMT.

Other studies (Barnes and Morozov, 2016; Zhu et al., 2019) have considered the variation in the internal structure geometrical configuration of spar caps & shear webs by altering the number and cross-sectional profile; a parametric elaboration of the results was put forward in relation to failure criteria. In detriment of the investigation methodology, however, was the absence of high-fidelity, transient loading conditions together with the implementation of a shell-element representation, rather than a solid-element representation. The stresses were hence induced solely along the perimeter of the cross-section, rather than acknowledged within a three-dimensional system. Fluid–structure interaction analyses have also been carried out by means of a monolithic-approach methodology, where the fluid dynamic and structural mechanic modules utilise subsequent results inherently in iterations (Zhang et al., 2014; Rafiee et al., 2016). These investigations, however, have either assumed the blade to be a solid structure, rather than varying designs or materials, or a shell representation implementing glass-fibre composite material properties.

Despite the undertaken research, a finite-element analysis of a real-scale high-solidity ducted rotor succumb to a variant distribution of static pressure and wall shear-stress along its surface due to the conditional parameters of an external fluid domain, at a free-stream vector both aligned and misaligned to the rotor axis, has not been attempted. This investigation evaluated the structural response of three distinct internal blade designs as a result of the hydrodynamic effects of the duct upon the rotor, where the individual blades were modelled as three-dimensional solid-element structures, rather than shell-element or plate-element structures. The numerical analysis elaborated in this present study is a continuation of Borg et al. (2020, 2021), which had developed real-scale CFD models to assess the hydrodynamic performance of a high-solidity, open-centre rotor within a bi-directional duct for tidal turbine applications.

2. Numerical methodology

2.1. Physical setup

In representation of the ducted high-solidity turbine, the dimensions described a duct radius (R_{dct}) of 7.5 m, a rotor radius (R_{rtr}) of 6 m,

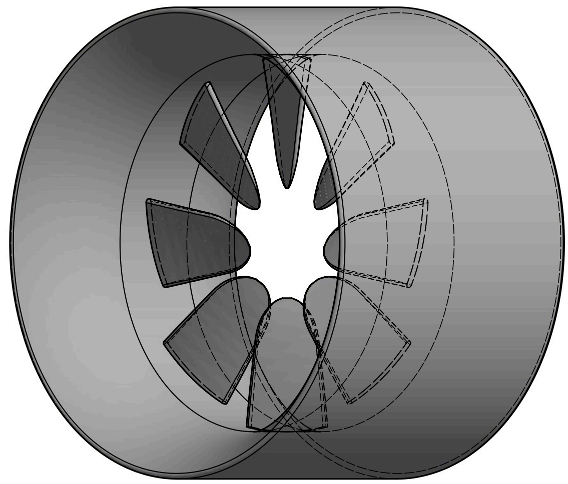

(a) Rendered three-dimensional CAD representation

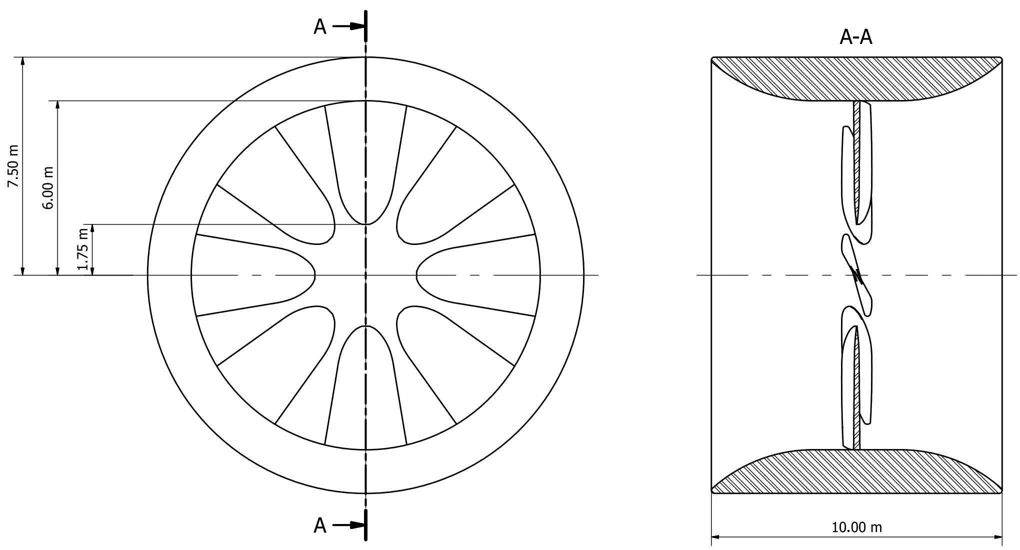

(b) First-angle sectioned projection

Fig. 2. Geometrical model of the ducted tidal turbine.

a hub radius (R_{hub}) of 1.75 m, and a duct length (L_{dct}) of 10 m, as illustrated in Fig. 2. The hydrofoil sections comprising the rotor blades consisted of a flat-plate design with rounded edges. The external hydrofoil geometry was quasi-identical to Allsop (2018), yet adapted to attain a more homogeneous blade surface. The geometry was provided by EDF R&D to replicate the outcomes of a turbine similar to the design of the OpenHydro PS2 device.

In view of the round-edged, flat-plate blade profile constituting the ducted rotor to acquire bi-directional turbine properties, an investigation into the most appropriate internal blade-structure design was instated. Due to the substantial chord-to-thickness aspect ratio, unique structural configurations may be required when compared to conventional slender blade designs. For this reason, in an effort to acquire an efficacious internal blade design in terms of specific mass, material cost, and structural response of the rotor blades, three design variations were investigated in replication of the designs elaborated in Krstulovic-Opara et al. (2009): (a) a solid blade consisting of a single material throughout its volume, (b) a cored blade consisting of a thick shell with a foam core, and (c) a reinforced blade consisting of a thick shell with webbing reinforcements in a void core, oriented perpendicular to the blade chord along the entire blade length, which has been water-flooded upon installation, as illustrated in Fig. 3. The implemented shell and reinforcement thicknesses of the two latter blade designs were instituted to be one-fourth of the blade profile thickness down the entire blade as a proximate median value from rotor composite cross-section evaluations by Grogan et al. (2013). In addition, the distance between each shear web reinforcement (d_{rein}) was acquired by means of:

$$d_{rein} = \frac{c_{rtr} - 2t_{rtr}}{3} \tag{1}$$

where c_{rtr} is the cross-section chord length and t_{rtr} is the cross-section thickness.

The materials considered for the structural analysis comprised of composite materials that are commonly utilised in the tidal turbine industry (Grogan et al., 2013): (i) double-biased (DB) orthotropic glass-fibre reinforced polymers (GFRP), employed for the solid blade design and the shell segments of the cored & reinforced blade designs; (ii) uni-directional (UD) anisotropic glass-fibre reinforced polymers, employed for the shear web reinforcement segments of the reinforced blade design; and (iii) corecell structural foam for the core segment of the

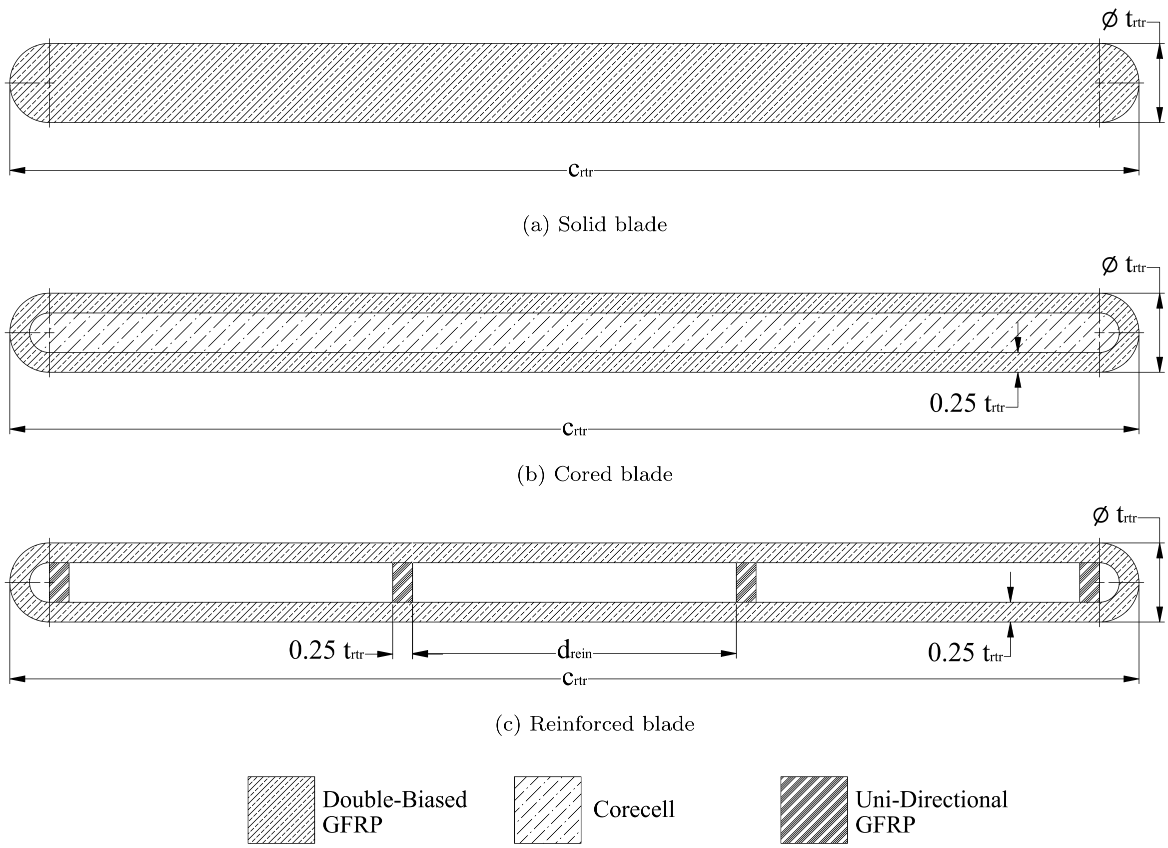

Fig. 3. Cross-sectional representations of the high-solidity rotor blade designs considered for the structural analyses.

Table 1
High-solidity rotor blade material properties (Grogan et al., 2013).

Material	E_1 (GPa)	E_2 (GPa)	G_{12} (GPa)	ν_{12}	Density (kg.m^{-3})	Design
DB GFRP	22.0	22.0	2.7	0.30	1850	a, b, c
Corecell	0.044	0.044	0.020	0.30	65	b
UD GFRP	38.8	10.0	2.7	0.28	1950	c

cored blade design. The properties of the listed materials are presented in Table 1.

A select range of hydrodynamic conditions was considered for the analysis. Within aligned flow conditions, low, mean, and extreme currents were considered at 1 m.s^{-1}, 4 m.s^{-1}, and 7 m.s^{-1}, respectively. In addition, a bearing range of 0°, 15°, 23.2°, 30°, solely at 4 m.s^{-1}, was considered within yawed flow conditions. Both analyses were conducted at low, nominal, and high rotational velocities (TSR 1.00, 1.75, and 2.50). The simulations implemented an inlet turbulence intensity of 3% and an inlet turbulent length scale of 1 m. At these conditions, the rotor designs were assessed on distinct criteria: (i) geometric characterisation, (ii) structural deflection, (iii) fracture response, (iv) capital cost, and (v) fatigue response to establish a definitive blade design selection for efficacious implementation within tidal turbine operation.

2.2. Numerical setup

A partitioned-approach fluid–structure interaction (FSI) model was set up, where the hydrodynamic solver was coupled with the structural solver by extracting the outcomes attained from the prior model and implemented as loading boundary conditions within the latter. In consideration of this technique, each of the rotor blades, disassociated from the duct, was individually modelled within the finite-element solver utilising the ducted turbine blade geometrical profiles employed within the fluid dynamic solver.

A one-way FSI analysis was favoured due to three factors: (i) the internal blade structure was required to be altered, hence varying the response properties of the structure; (ii) the non-slender physicality of the high-solidity blades may exhibit high structural stiffness; and (iii) as the extremities of the blades are fixed at the duct, where the highest dynamics are induced, the structural response may not be significant. Due to the incorporation of a one-way approach, the loading data was therefore identical for each blade design upon implementation.

2.2.1. Partitioned-approach fluid–structure framework

In an effort to constitute the one-way fluid–structure interaction framework, the boundary conditions inducing a loading distribution along the blade surfaces were instated from the distributions of static pressure and wall shear-stress attained within, and imported directly from, the hydrodynamic model at distinct temporal points along the turbine rotation. The hydrodynamic model described a three-dimensional, real-scale, unsteady CFD model that coupled the seven-equation Reynolds-Stress 'Stress-Omega' Model (τ-ω) turbulence model to close the Navier–Stokes equation and analyse the anisotropic flow domain (Wilcox, 2006). The structural model described a solid three-dimensional quasi-static model. Each of the eight blades was modelled independent from the entire system, upon which unique loading conditions were imposed.

The partitioned coupling from the hydrodynamic solver to the structural solver consisted of exporting data points detailing the Cartesian location and value of the parameters specified. As the total force induced by a fluid flow is the summation of static pressure and wall shear-stress upon a surface, the two parameters were extracted from the CFD solver. Within the finite-element model, static pressure was imposed as a magnitude, whereas wall shear-stress was imposed as

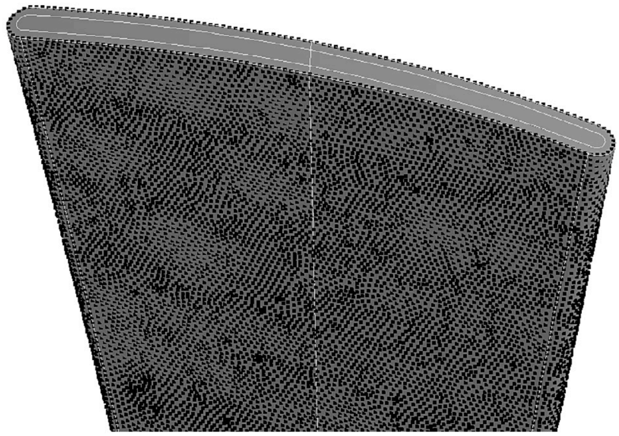

(a) Distribution of input source points along the blade surface

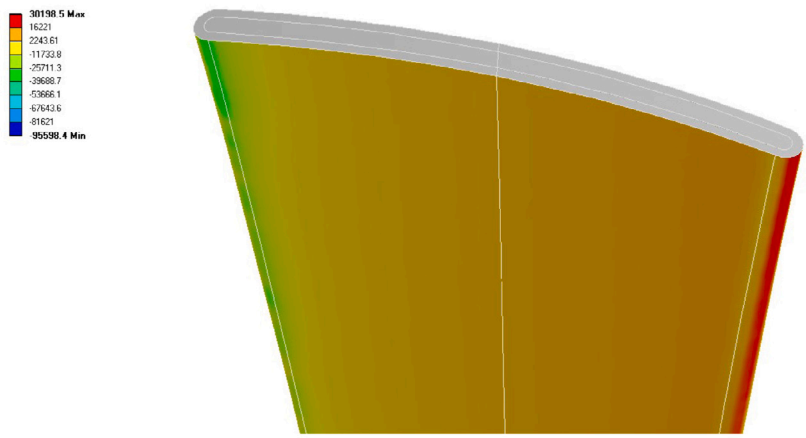

(b) Static pressure input boundary condition ($U_\infty = 7$ m.s^{-1}; $TSR = 1.75$; $\phi = 0^o$)

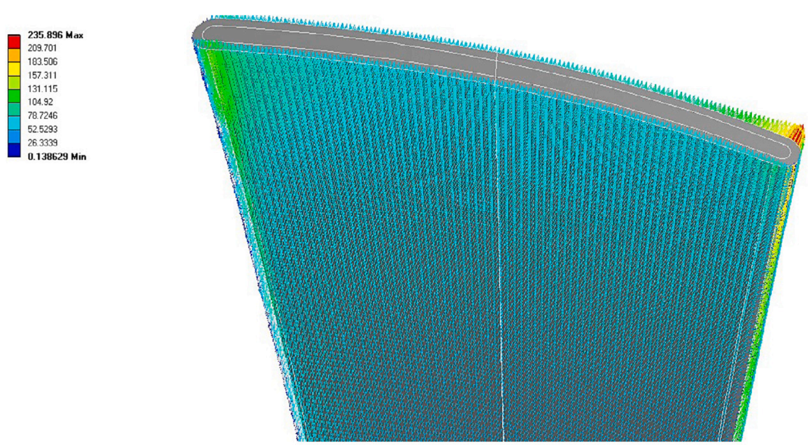

(c) Wall shear-stress input boundary condition ($U_\infty = 7$ m.s^{-1}; $TSR = 1.75$; $\phi = 0^o$)

Fig. 4. Illustration of the partitioned-approach fluid–structure interaction technique implementation by importing parameter distributions along the blade surface from the hydrodynamic CFD model.

a Cartesian vector (x-,y-, and z-wall shear). On average, 55,000 data points per time-step were transferred; the implementation is illustrated in Fig. 4. The parametric distribution at the rotor surface was imported at every azimuth angle (ϕ) of 45° along the rotation for three periods to attain a representation of the dynamic load induced upon operation.

In addition to the hydrodynamic parameters, hydrostatic pressure was introduced within the solution by modelling the rotor axis to be situated 20 m below sea-level due to the ducted tidal turbine design conditions of being installed at 35 m depth (Zhou et al., 2017). Furthermore, fixed boundary conditions were allocated to the root surface of the blade, together with Coriolis effect considered at constant

Table 2
Mesh independence analysis for the solid/cored rotor blade structural design.

n	Cell number	Cell number ratio	S	ε	Ψ
3	635,672	1.242	0.002528	−0.000030	0.2451
2	511,834	1.340	0.002498	−0.000122	
1	382,167		0.002376		

rotational velocity, to acquire representative environmental conditions of the ducted, high-solidity tidal turbine in operation.

2.2.2. Finite-element mesh

Designed to explicitly incorporate all eight distinct rotor blades for the three blade designs, the physical models were imprinted with a hybrid hexahedral–tetrahedral mesh for the solid and cored blade designs, and a hexahedral mesh for the reinforced blade design, illustrated in Fig. 5. The physical models consisted of solid quadratic elements. The implementation of solid elements was preferred in representing the outer-shell segment of the blade as shell elements put forward the assumption that the structural outcomes are consistent throughout the structure thickness. This was deemed to be untenable for the full-scale high-solidity rotor due to the complex geometrical layout of the blade, together with the variable parametric distribution upon its surface.

In addition to a solid-element format, quadratic elements were utilised to introduce mid-nodes within each cell. The implementation was advantageous in discretising the thickness of the outer-shell & reinforcement structures to increase the accuracy of the simulation. Furthermore, a two-cell-thick layout was imposed along the thickness of the shell & reinforcement sections, as illustrated in Fig. 5(b), to attain a quadratic relationship between the structural outcomes and the thickness of the blade feature; hexahedral volumetric cells were imposed along the load-bearing surfaces for all blade designs.

In creating the mesh, the solid and cored blades were instated as whole components for the cells to be imposed along; identical meshes were utilised, yet differing material properties were allocated for the two designs. The reinforced blade, however, was more complex to set up. To permit an equivalent distribution of hexahedral cells, the structure was discretised into blade sections. Yet, due to the discretisation, the three-dimensional non-uniform rational basis spline (NURBS) sectioned structure was too complex to tessellate in a consistent manner. In consequence, the sections were meshed separately, and numerically linked by means of a face-to-face bonded contact merge when simulating. Overall, the eight rotor blades were meshed, where the solid/cored rotor mesh was comprised of a total of 635,672 elements and 2,680,248 nodes, whereas the reinforced rotor comprised of 571,392 elements and 3,362,160 nodes. A mesh independence procedure, described in Table 2, was carried out on the rotor designs by considering the parameter with the highest degree of dynamics. Mesh independent parameters were established utilising ITTC recommended meshing procedures and guidelines (Resistance Committee of the 28th ITTC., 2017):

$$\varepsilon_n = S_n - S_{n-1} \tag{2}$$

$$\Psi = \frac{\varepsilon_n}{\varepsilon_{n-1}} \tag{3}$$

where Ψ is the convergence ratio, ε is the difference between the considered variable (S) at different mesh independence study iterations, and the subscript n is the mesh independence study iteration.

The finite-element computations were performed using the ARCHIE-WeSt cluster facility at the University of Strathclyde by running two Intel Xeon Gold 6138 2.00 GHz computational nodes, with 8 cores and up to 192 GB of RAM per node per simulation. One ducted rotor structural simulation was completed within roughly 20 wall-clock hours, equivalent to 160 core-hours.

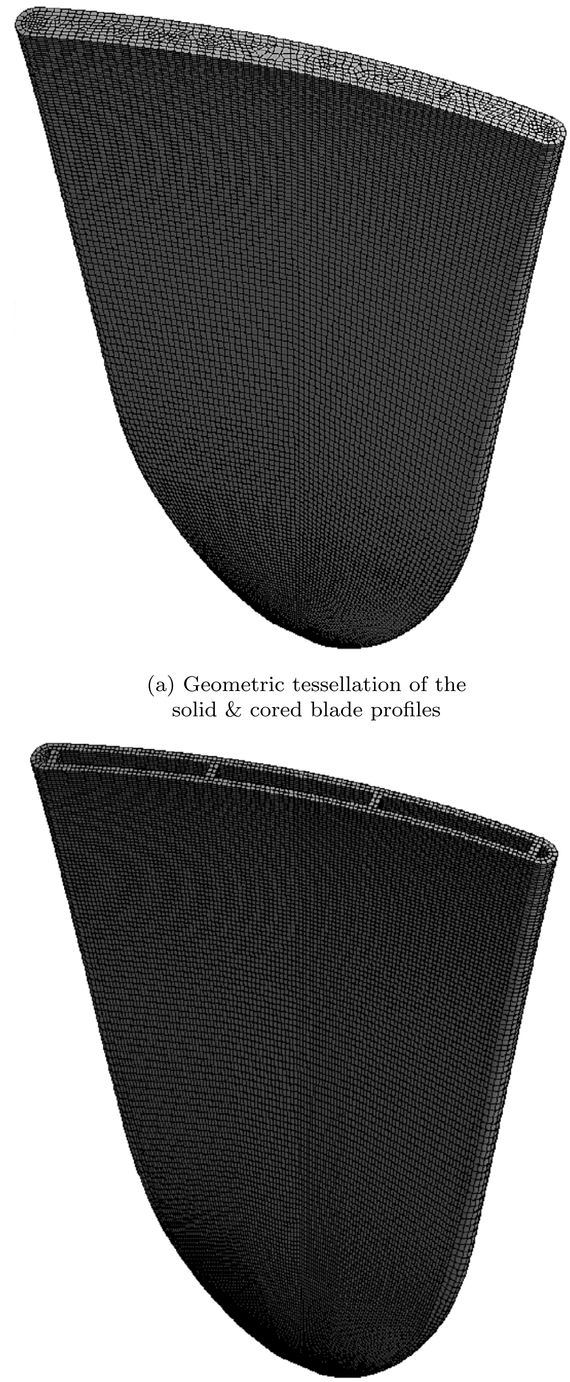

(a) Geometric tessellation of the solid & cored blade profiles

(b) Geometric tessellation of the reinforced blade profile

Fig. 5. Illustration of the blade meshes.

3. Numerical model characterisation

3.1. Physical modelling

In consideration of the analysis of a physical turbine, notable definitions concerning the resultant performance outcomes were identified. The tip-speed ratio (TSR) was established as an equivalence between the linear blade-tip velocity and the free-stream velocity (U_∞):

$$TSR = \frac{\Omega_x R_{rtr}}{U_\infty} \tag{4}$$

Table 3
Geometric properties of the high-solidity tidal turbine rotor designs.

Blade property	Solid design	Cored design	Reinforced design
Moment of Inertia (kg.m^2)	4.587×10^5	2.422×10^5	3.640×10^5
Specific Mass (kg.m^{-3})	1850	982	1472
Specific Gravity	1.853	0.984	1.475

where Ω_x is the system axial rotational speed and R_{rtr} is the rotor radius.

The thrust coefficient (C_T) was quantified as a function of the device thrust (T_{dvc}) and the maximum thrust potentially induced upon the device area (T_∞):

$$C_T = \frac{T_{dvc}}{T_\infty} = \frac{F_z}{\frac{1}{2}\rho A_{dvc} U_\infty^2} = \frac{F_z}{\frac{1}{2}\rho \pi R_{dvc}^2 U_\infty^2} \tag{5}$$

where ρ is the fluid density, A_{dvc} is the device area, R_{dvc} is the device radius, and F_z is the stream-wise axial force on the device.

In establishing the fatigue life of the materials constituting the blades, the strain-life method was utilised to relate the temporal structural response:

$$\frac{\Delta\varepsilon_e}{2} = \frac{\sigma'_f}{E} \cdot (2N_f)^b \tag{6}$$

where $\Delta\varepsilon_e$ is the total strain amplitude, σ'_f is the fatigue strength parameter, E is the Young's modulus, N_f is the number of cycles to failure, and b is the fatigue strength exponent.

4. Structural performance of the ducted, high-solidity tidal turbine rotor

4.1. Geometric characterisation

Primarily acknowledging the variations in geometric characteristics between the blade designs, three properties were investigated: the moment of inertia, specific mass, and specific gravity of the high-solidity rotors.

As specified in Table 3, the solid blade design attained the highest parametric values. This design required the highest degree of torque to induce a unit rotational acceleration. In contrast, the cored blade design attained the lowest parametric values as half of the dense GFRP volume was substituted for the Corecell material. The reinforced design, consisting of two GFRP materials for the shell and webs, whilst flooded with water, presented intermediate values between the two prior designs.

4.2. Hydrostatic analysis

Hydrostatic pressure was implemented along the surfaces of the blades in simulation of the subsea depth. The suitability of the structures was therefore acknowledged throughout non-operational procedures, such as installation and maintenance processes.

By means of the analysis, the solid and reinforced blade designs sustained their structural integrity as no structural deviation was induced. The cored blade, however, was succumb to minute yielding, due to the malleable foam-core, which induced a region of low strain at the root, as illustrated in Fig. 6.

4.3. Hydrodynamic performance analysis

The hydrodynamic thrust induced upon the ducted turbine rotor during operation within aligned and yawed flow conditions was analysed, as illustrated in Fig. 7(a) and Fig. 7(b), respectively. Within aligned flow conditions, a high thrust coefficient was attained at low TSR, with a mean value of 0.76, which decreased to a mean of 0.52 at high TSR in a linear variation. The outputs at yawed flow conditions acted similarly, yet portrayed a deviation dependent on the angular bearing of the free-stream. The highest thrust was attained at a flow-bearing of 23.2^o. Further descriptions are elaborated in Borg et al. (2020).

4.4. Hydrodynamic fracture analysis

4.4.1. Blade deflection

4.4.1.1. Axial deflection. Primarily, the blade deflection acting parallel to the rotor axis was analysed in relation to the free-stream magnitude and turbine rotational velocity for all three blade designs. Illustrated in Fig. 8, the solid blade attained the lowest mean deflection, whereas the cored blade acquired the highest, albeit minutely, due to the implementation of the foam core, which constituted 50% of the blade volume, diminishing the global Young's modulus. The reinforced blade attained an intermediate mean deflection.

The axial deflection was relatively minute for all three designs, with a maximum deflection equivalent to approximately 4% of the blade length. The deflections were minute as the blade was constrained at the tip, where higher dynamics were induced, rather than at the hub. At yawed flow conditions, the deflections of the blade were more substantial at higher TSRs, as illustrated in Fig. 9, analogous to the variation in thrust.

The behaviour of the deflection along the blade surface was investigated. As illustrated in Fig. 10, the maximum value was attained at the trailing edge in the vicinity of the blade hub. The point of highest deflection was present at this location as a result of the relatively high blade pitch, inducing simultaneous bending and torsion upon the structure.

4.4.1.2. Global deflection. To acknowledge the proportion of axial deflection upon the full physical response, the three-dimensional global deflection of the blades was acquired, illustrated in Fig. 11. On average, for both aligned and yawed flow conditions, the axial deflection was found to be approximately 94% of the total deflection, hence acknowledging the majority of the dynamics induced to be acting within the axial direction of the rotor.

4.4.2. Normal elastic strain

4.4.2.1. Radial strain. Establishing the strain acting along the length of the blades, the lowest values of radial strain were attained by the solid blade design, as illustrated in Fig. 12. The highest values were displayed by the cored blade due to the comparably lesser rigidity, with an intermediate value by the reinforced blade. The maximum radial strain along the blade diminished with rotational velocity, yet increased in relation to the free-stream velocity, analogous to the thrust variation induced upon the blade. The cored design response at low free-stream conditions was acknowledged to be distinct from the supplementary two blade designs due to the strain instigated by the hydrostatic pressure. In addition, the maximum strain response induced at yawed flow conditions occurred at flow bearings of 15° and 23.2° for all blade designs, as depicted in Fig. 13.

The highest tensile value transpired upon the cored blade at low rotational velocity in extreme free-stream conditions. The magnitude was 22.1% of the DB GFRP yield strength, hence not exceeding its ultimate strain-to-failure value. To ascertain its structural integrity, an engineering safety factor of 2 was implemented, increasing the normal strain to 44.2% of the permissible strain. Operation at the specified conditions was therefore inconsequential to the structural integrity of the rotor, and within the limits of reliable operation.

Furthermore, in recognising the radial strain distribution along the surfaces of the three blade designs, illustrative representations of the structures were established, as depicted in Fig. 14. By means of the analysis, two strain concentrations, in tension and compression, were acknowledged towards the leading edge, at the root, of the high-solidity blade for all three structural designs in both aligned and yawed flows. The concentration was brought about due to the simultaneous bending and torsion instigated by the fluid–structure interaction upon the wide blade. Consequent to the presence of strain localisation, should a structural defect transpire, crack propagation may induce the structural failure of the high-solidity blade.

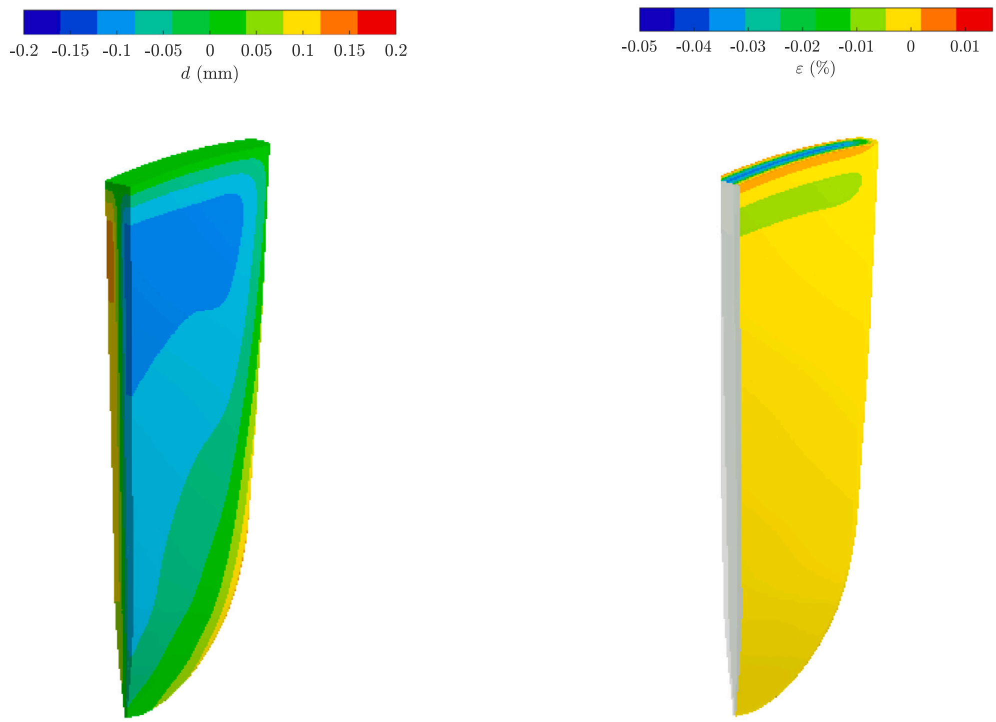

(a) Axial deflection (b) Radial strain distribution

Fig. 6. Structural response cross-section of the cored blade design under hydrostatic load.

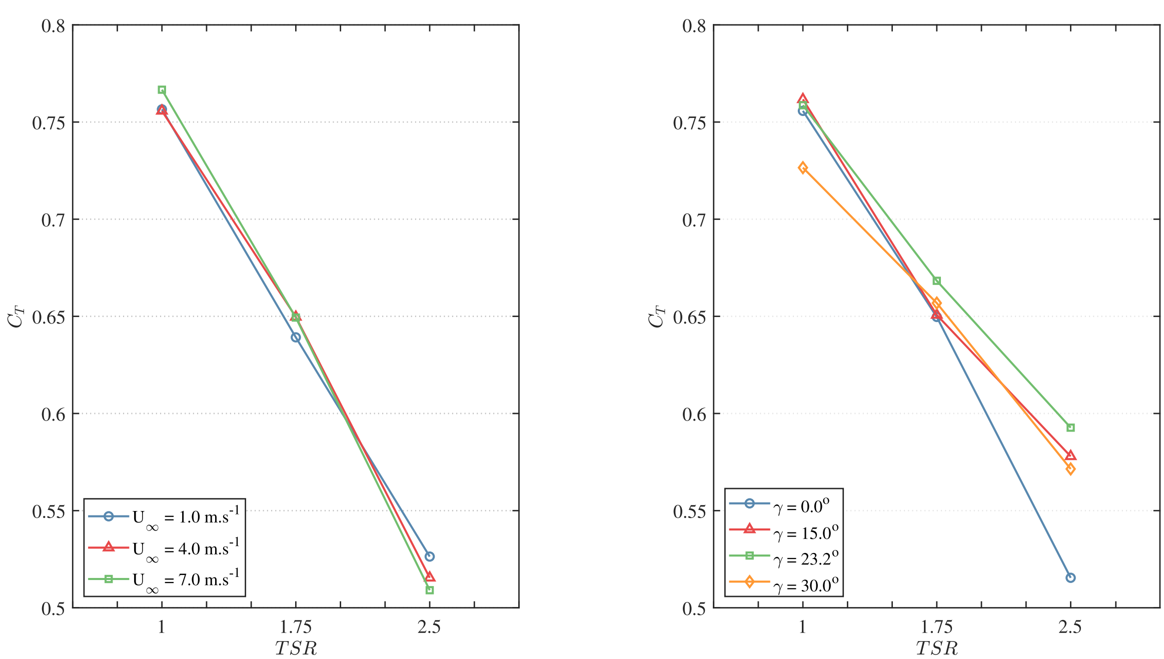

(a) Aligned Flow Conditions (b) Yawed Flow Conditions

Fig. 7. Mean hydrodynamic thrust coefficient upon the turbine rotor at aligned and yawed flow conditions.

In addition, the illustrated surface strain distribution of the three blades were distinct in relation to the internal design. The solid design attained a comparatively large concentration zone, which dissipated gradually along the structure. The cored design sustained a higher degree of strain concentration along the root of the rotor blades. The reinforced design permitted global strain reduction, yet induced local strain increases at the locations of the reinforcement webs.

4.4.2.2. Tangential strain & axial strain. Identifying strain acting along the width of the blade, illustrated in Fig. 15, the values of tangential strain were found to be, on average, a magnitude of 3, for solid blades, and 15, for cored and reinforced blades, lower than the radial strains. The lowest values of tangential strain were attained by the reinforced blade design, whereas the highest values were displayed by the solid blade design. Due to the orthotropic material consistency of the blade

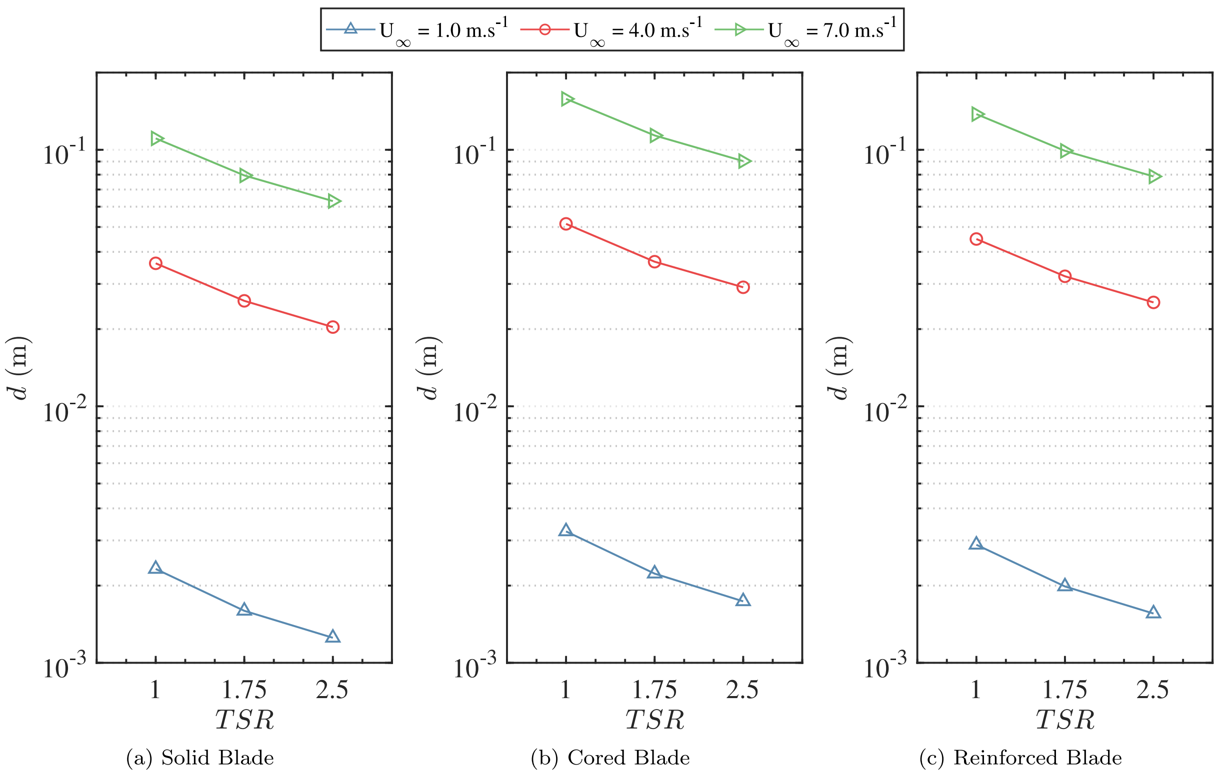

Fig. 8. Mean axial deflection of the distinct blade designs within aligned flow conditions.

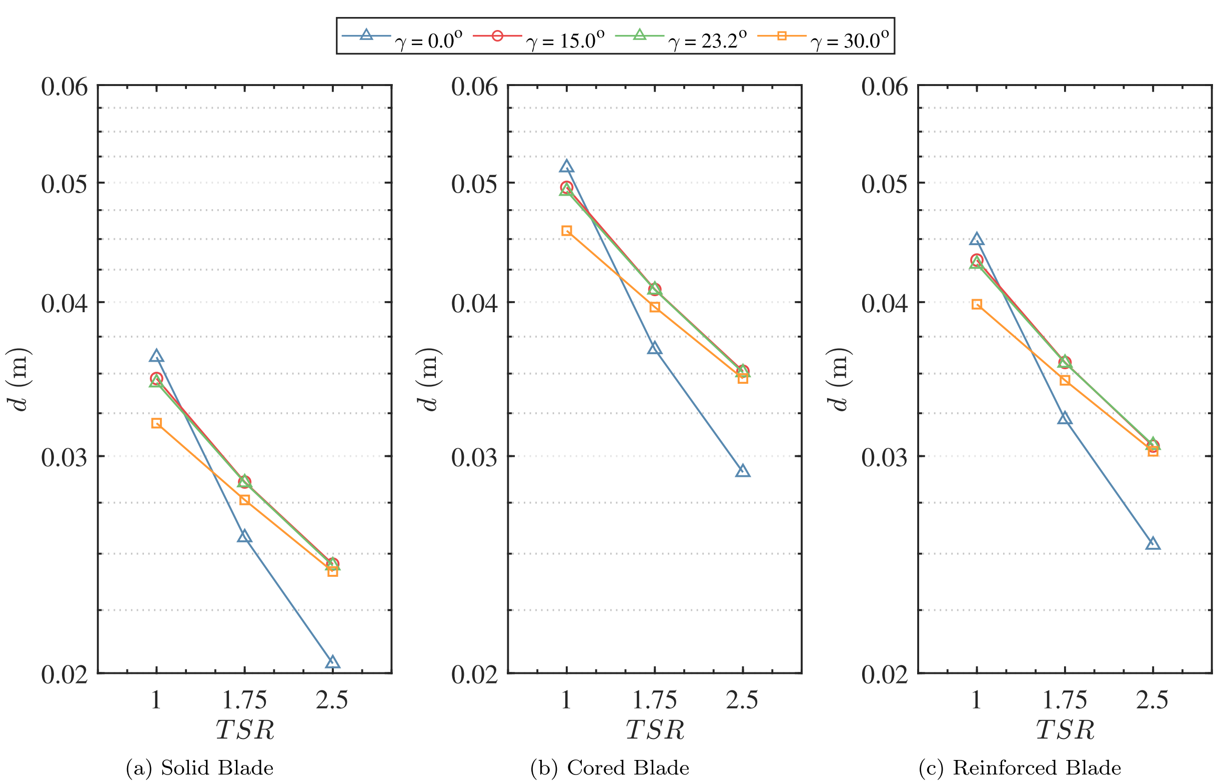

Fig. 9. Mean axial deflection of the distinct blade designs within yawed flow conditions.

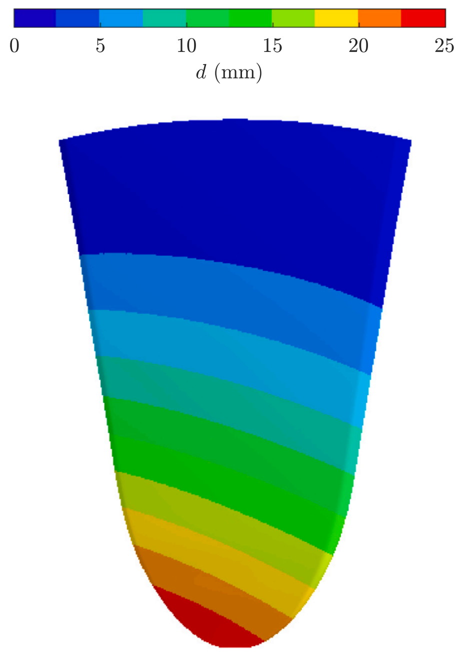

Fig. 10. Illustration of the axial deflection distribution along the solid blade design ($U_{\infty} = 4$ m.s^{-1}; $TSR = 1.75$; $\phi = 0°$).

setup, the higher rigidity permitted lessened stress dissipation in comparison to the variant designs. Similar to the variation in hydrodynamic thrust induced upon the blade, the tangential strain along the blade diminished with rotational velocity, whilst increasing with free-stream velocity.

Identifying strain acting in a direction parallel to the rotor axis, illustrated in Fig. 16, the values of axial strain were found to be, on average, a magnitude of 3, for solid blades, and 13, for cored and reinforced blades, lower than the radial strain. The variations in structural outcomes displayed similarities with those of tangential strain.

4.4.3. Equivalent elastic strain

As the structural response of the high-solidity rotor pertained multidirectional strain states, the von Mises equivalent elastic strain was analysed. The lowest values of equivalent strain were attained by the solid blade design, whereas the highest values were displayed by the cored design due to the lesser rigidity. The reinforced design attained an intermediate response, as illustrated in Fig. 17. As a result of the degree of strain, the maximum tensile value increased to 67.8% of the DB GFRP yield strength.

4.4.4. Shear elastic strain

The ducted tidal turbine design consisted of rotor blades sharply extruding from the duct housing at the tip of the structure, where dynamics are highest. The induced shear strain was therefore investigated at the interfacing plane between the blade root and the duct.

Illustrated in Fig. 18, the value of shear response was found to be equivalent in magnitude to the equivalent strain, as the strain concentrations were present within the vicinity of the blade root. The shear distribution along the root plane at mean aligned velocity was investigated for the three blade designs, illustrated in Fig. 19. Along the three blade profiles, four concentration zones were developed at the rounded vertices of the root plane as torsion and bending motions were induced.

4.5. Material cost analysis

In result of the outcomes attained via the prior investigations, the structural integrity of the three proposed internal blade designs was sustained within the analysed conditions. To establish a distinction between the designs, a material cost analysis was put forward,

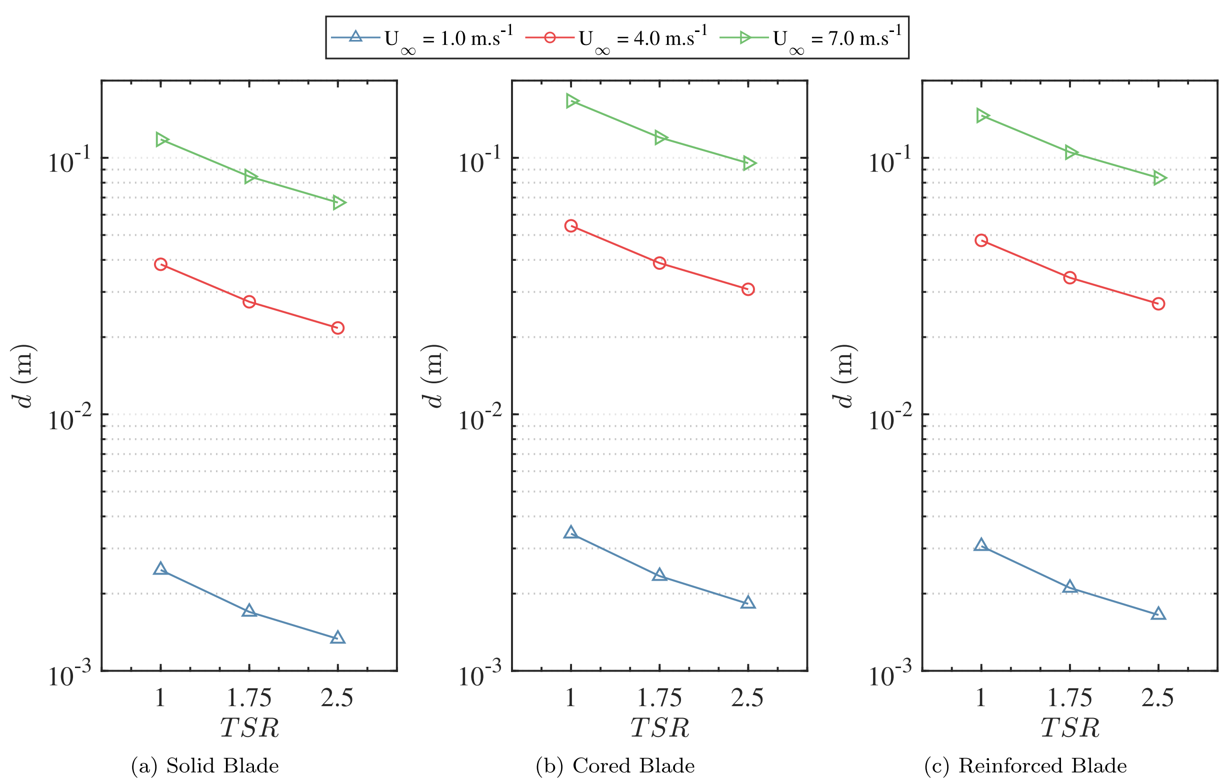

Fig. 11. Mean global deflection of the distinct blade designs within aligned flow conditions.

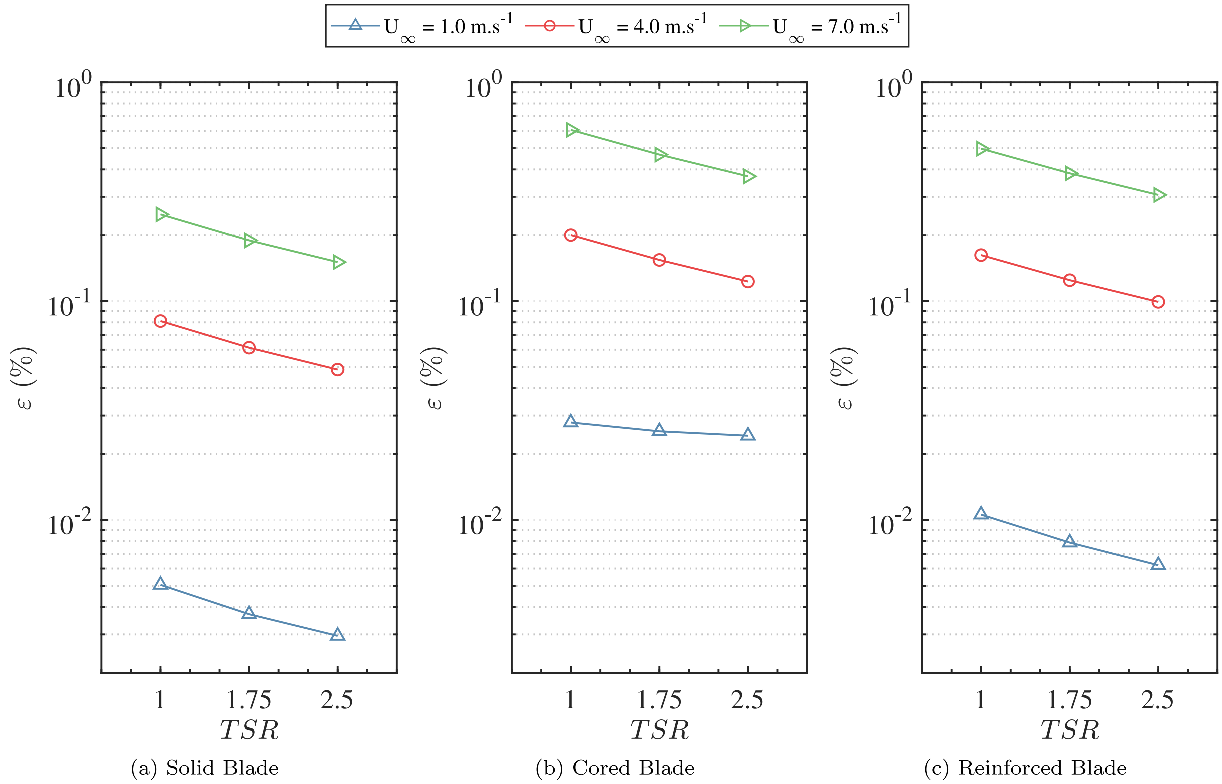

Fig. 12. Mean normal radial strain of the distinct blade designs within aligned flow conditions.

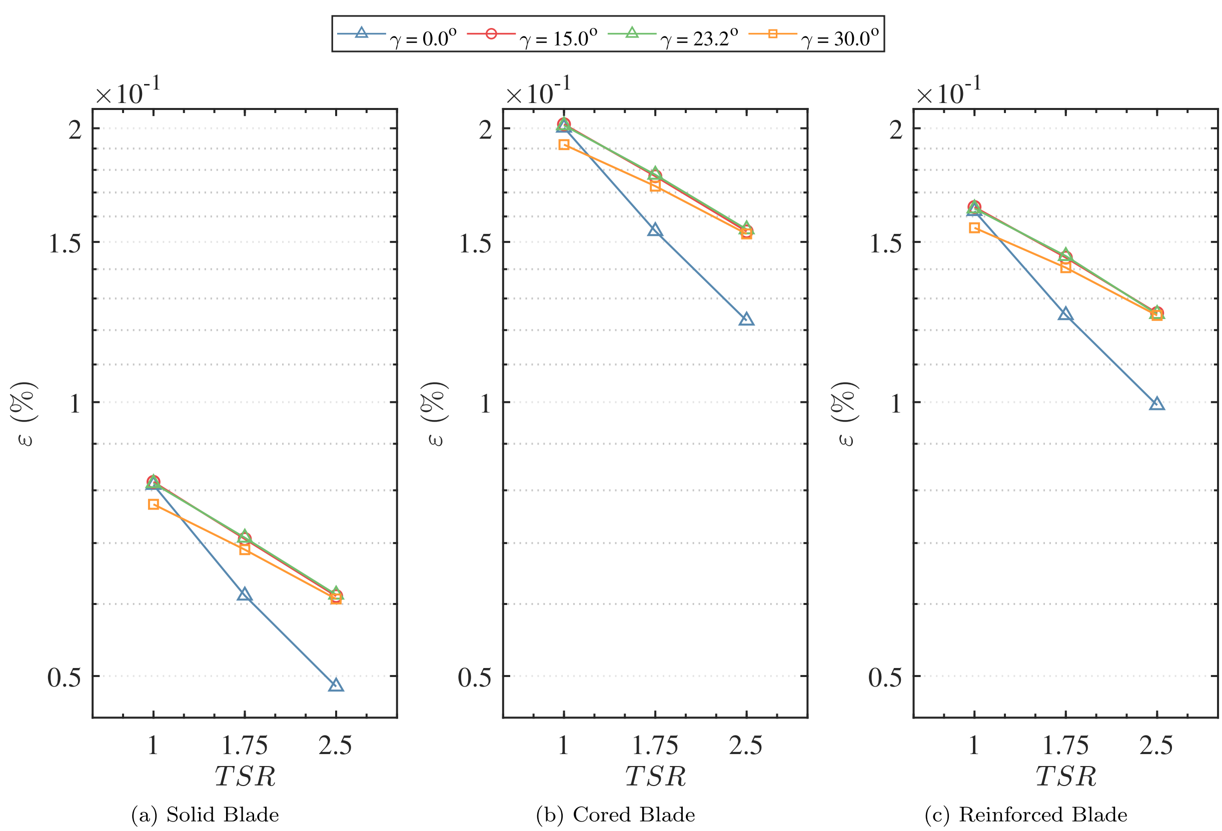

Fig. 13. Mean normal radial strain of the distinct blade designs within yawed flow conditions.

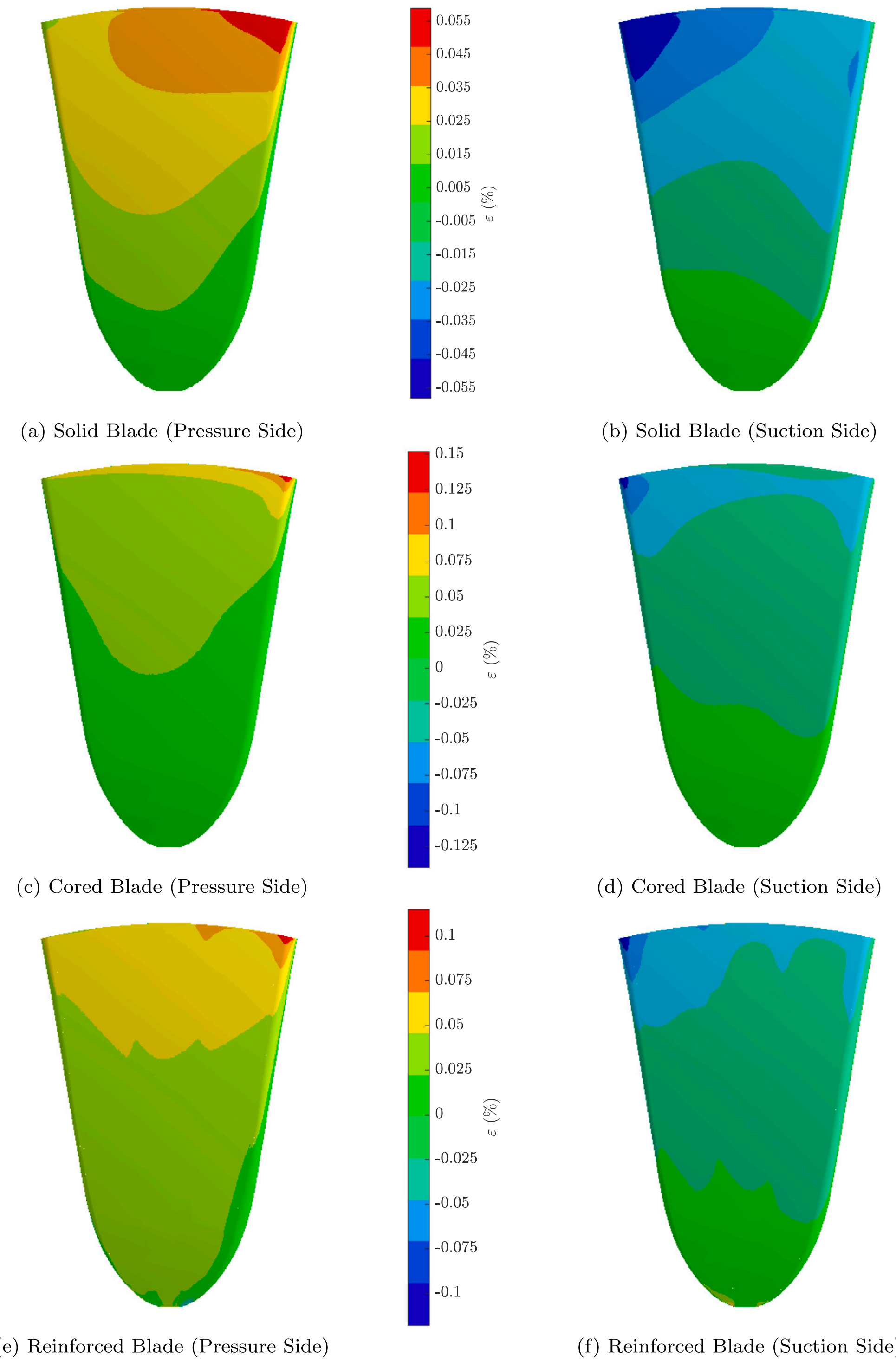

(a) Solid Blade (Pressure Side) (b) Solid Blade (Suction Side)

(c) Cored Blade (Pressure Side) (d) Cored Blade (Suction Side)

(e) Reinforced Blade (Pressure Side) (f) Reinforced Blade (Suction Side)

Fig. 14. Illustrations of the normal radial strain distribution along the blade structural designs ($U_\infty = 4$ m.s^{-1}; $TSR = 1.75$; $\phi = 0°$).

acknowledging the most cost-effective composition, in exclusion of manufacturing and fabrication costs.

Implementing material costs for uni-directional fibre sheets, bi-directional fibre sheets, epoxy resin, and structural foam materials from prior investigations (Bortolotti et al., 2019), whilst attaining the volume of the blade components from the established structural model, the final costing estimations of the blade materials for the full rotor was established, as depicted in Table 4. The ratio of filler-to-matrix materials within the GFRPs was acquired by relating the densities of the matrix (Solvay, 2013) and e-glass to the global density of the fibreglass material. The most cost-effective arrangement, in terms of materials implemented, was found to be the reinforced design, being approximately 50% and 6.5% lower in capital than the solid and cored blade designs, respectively.

4.6. Fatigue analysis

4.6.1. Principal elastic strain

In establishing the characteristics that lead to temporal failure as a result of fatigue crack propagation, the maximum principal strain

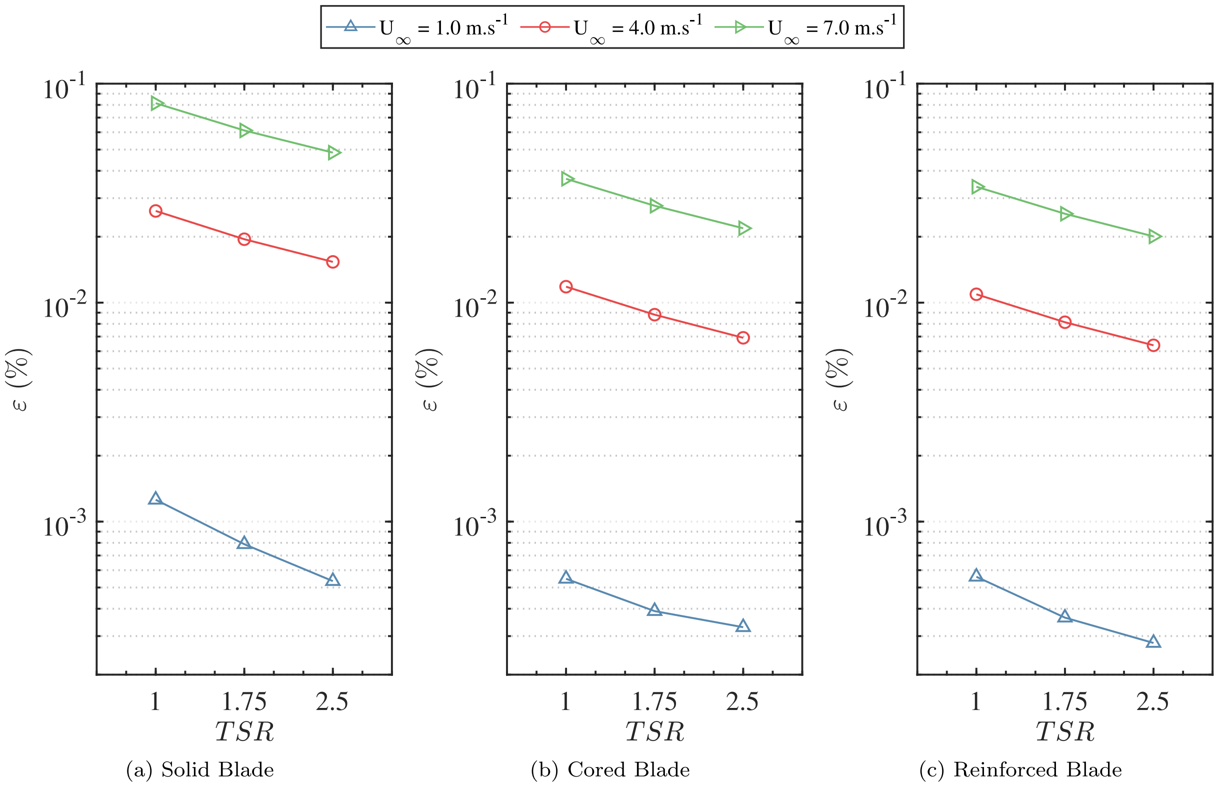

Fig. 15. Mean normal tangential strain of the distinct blade designs within aligned flow conditions.

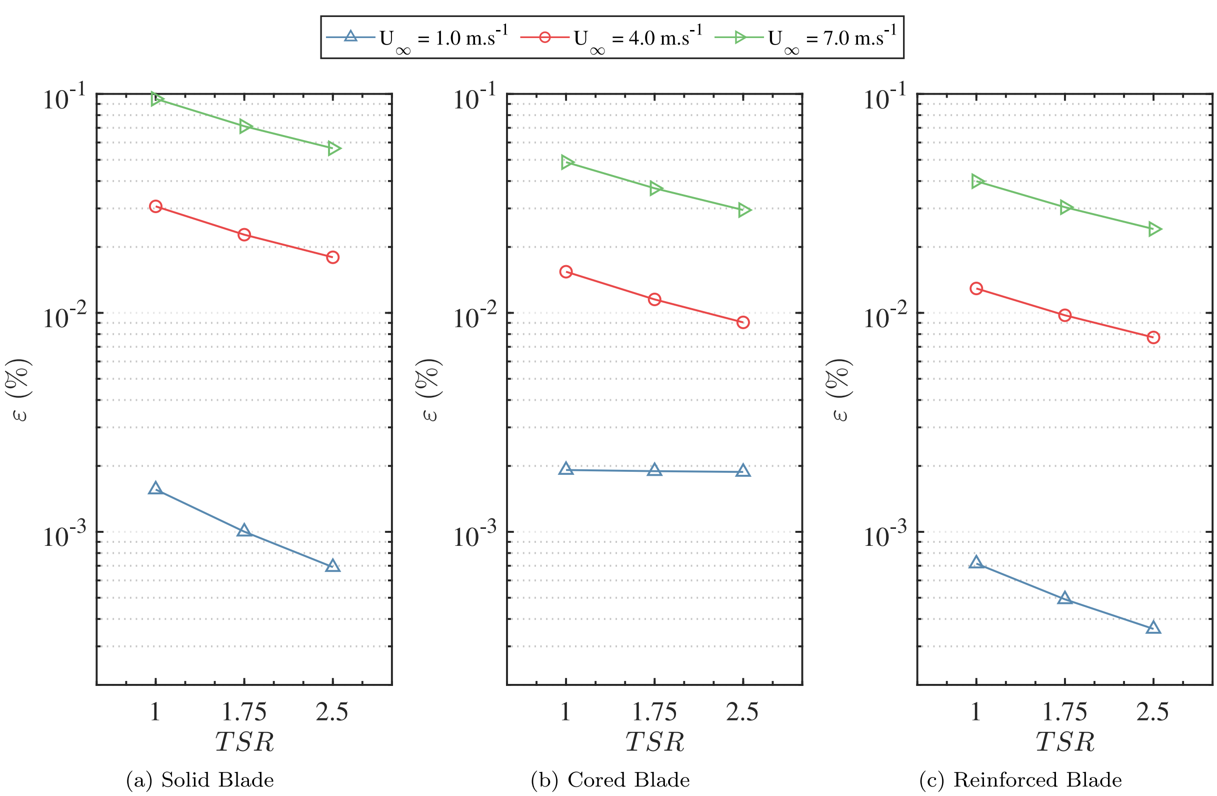

Fig. 16. Mean normal axial strain of the distinct blade designs within aligned flow conditions.

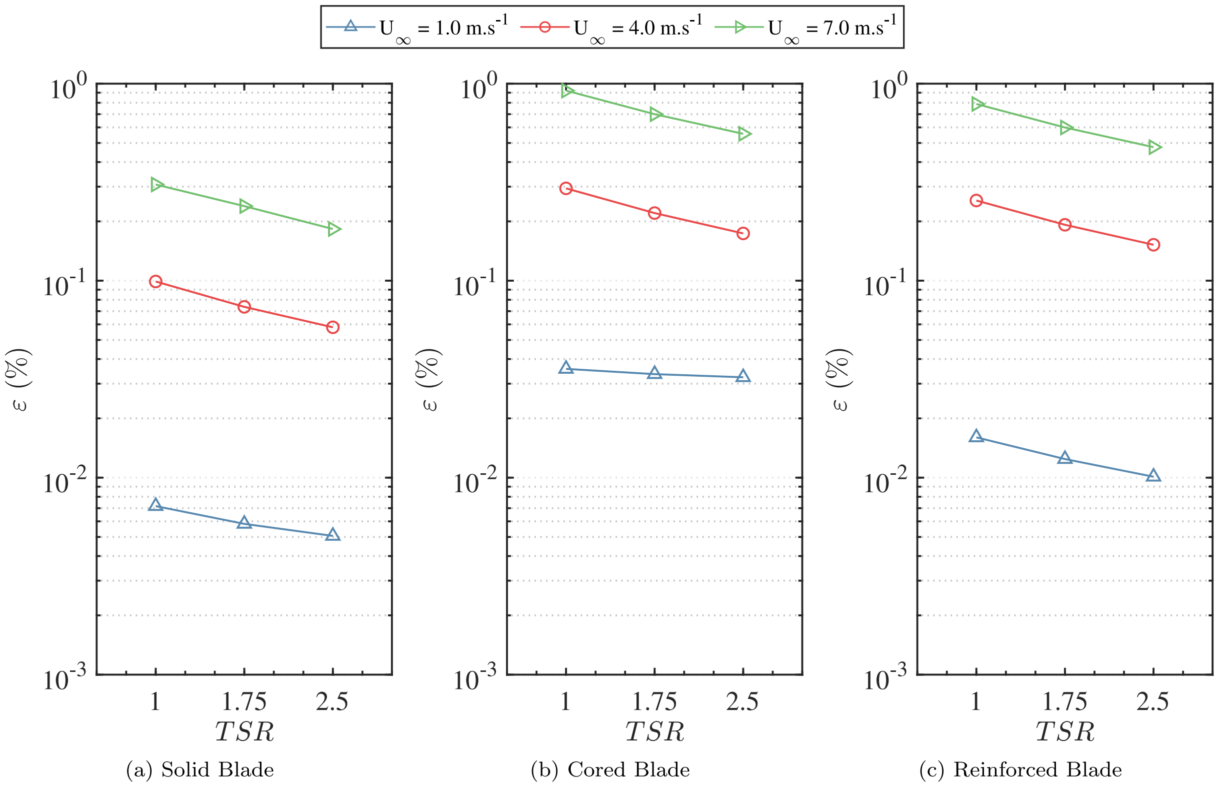

Fig. 17. Mean equivalent strain of the distinct blade designs within aligned flow conditions.

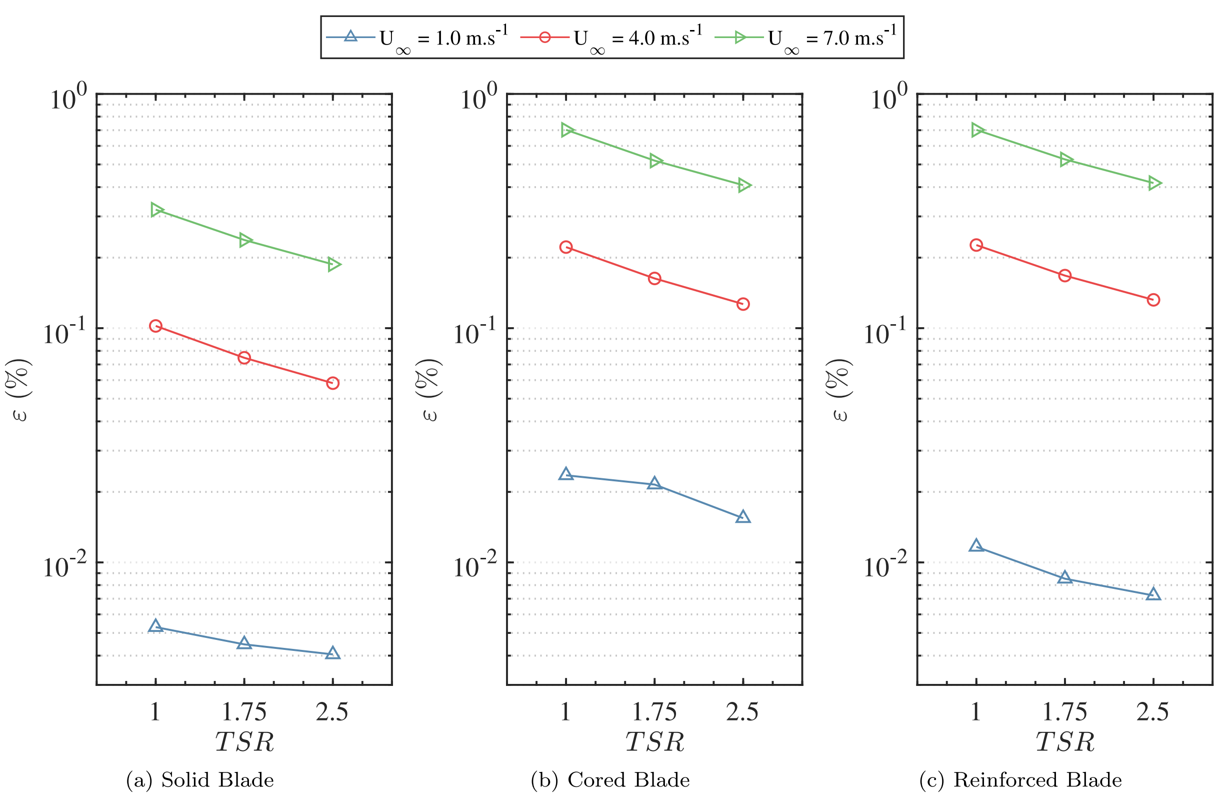

Fig. 18. Mean shear strain of the distinct blade designs within aligned flow conditions.

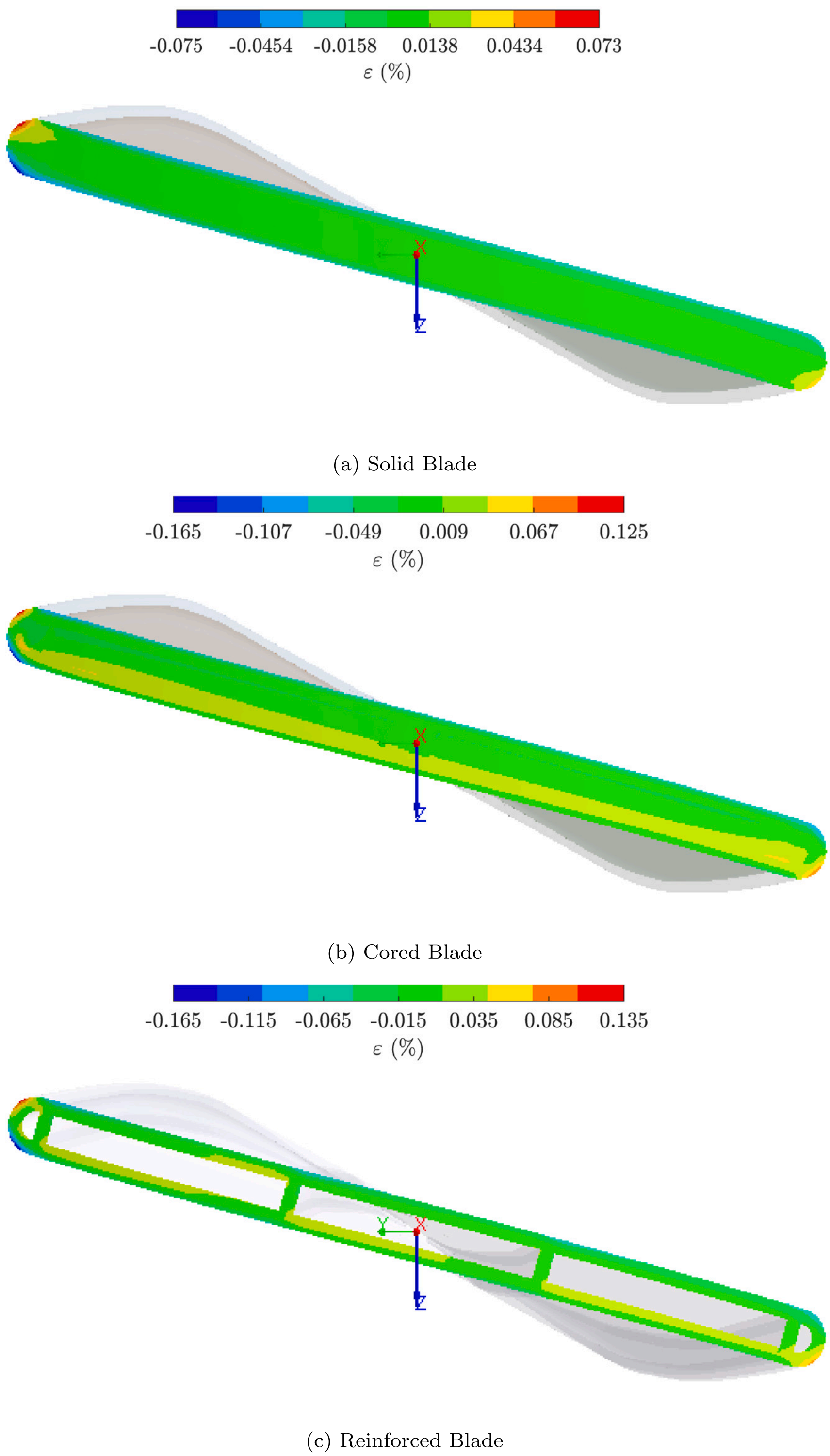

Fig. 19. Illustrations of the shear strain distribution at the blade root ($U_{\infty} = 4$ m.s^{-1}; $TSR = 1.75$; $\phi = 0°$)

along the blade was investigated. Analysed at the mean free-stream magnitude (4 m.s^{-1}) within aligned (0°) and nominal bearing (23.2°) at mid and high rotational velocities, the mean response per azimuth angle of 45° was attained. Due to the inconsistencies in the strain response of the cored blade design at low free-stream velocity, the fatigue analysis was solely undertaken upon the solid and reinforced blade designs. By means of the investigation, a cyclic response was acknowledged, as illustrated in Fig. 20, providing evidence of the likelihood of failure by fatigue.

4.6.2. Strain-life analysis

As a cyclic load was induced within a rotational period of power-generating operation, an investigation into the fatigue performance of the fibre-composite rotor blade designs was carried out. Analysing the

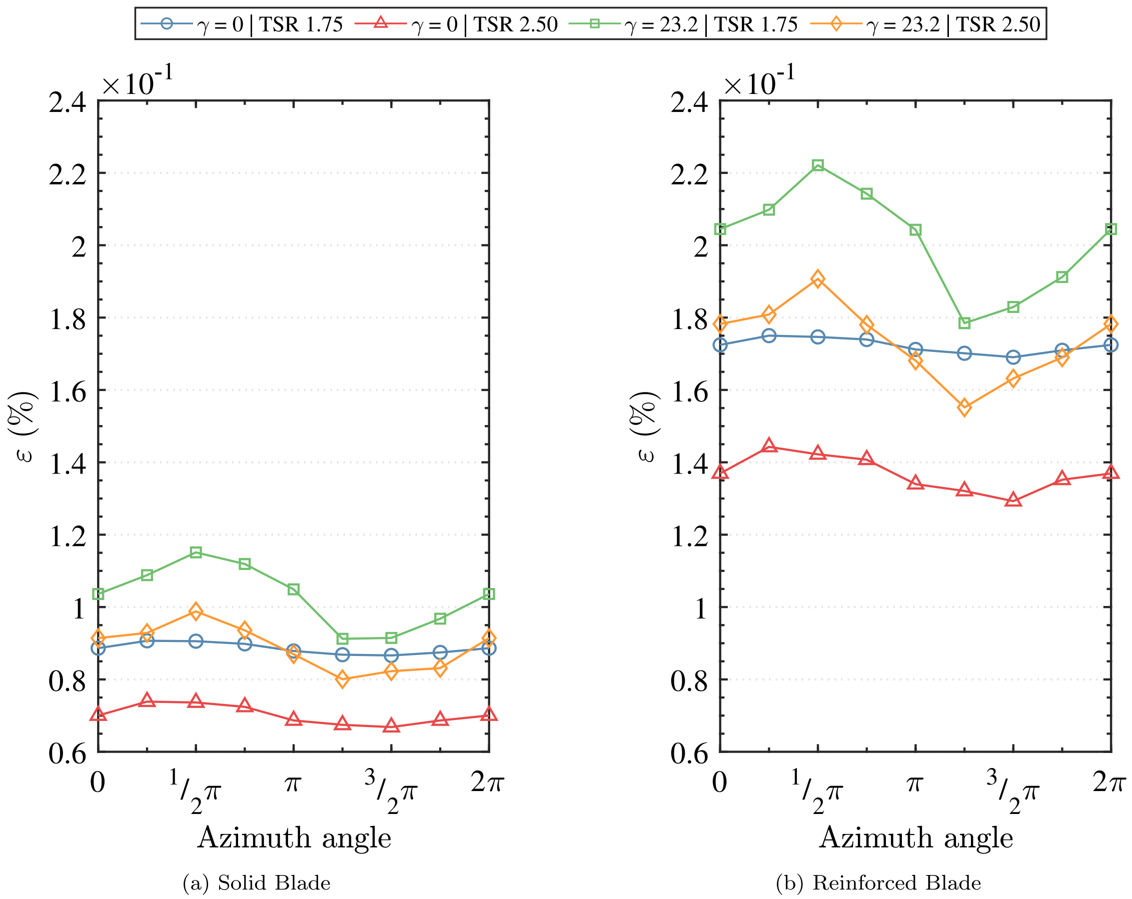

Fig. 20. Cyclic representation of maximum principal elastic strain within aligned and yawed flow conditions.

Table 4
Total material costs of the high-solidity tidal turbine rotor designs.

Blade structure	Solid design	Cored design	Reinforced design
Cost ($)	596,000	321,000	300,000

system when succumb to high-cycle fatigue, the strain-life (ε_e - N_f) methodology was implemented to establish the temporal response of the ducted turbine rotor within a 10- to 25-year design-life.

The strain-life approximation however requires specifications related to the failure properties of the material utilised, namely the fatigue strength exponent (b) and fatigue strength parameter (σ_f'), to acquire the strain fluctuation that induces failure by fatigue within a number of cycles. The two values are typically established by means of experimentation in relation to destructive testing, which were not known for the adopted composite material. In this regard, as the supplementary terms within the strain-life equation were acquired, the methodology was therefore utilised to establish a definitive material property range to avoid failure by fatigue. The equation was satisfied by implementing the mean variation in principal elastic strain per cycle ($\Delta\varepsilon_e$) acquired via the finite-element analysis, Young's modulus (E), and number of cycles to failure (N_f) established to vary between 10 to 25 years of operation within Paimpol-Bréhat site conditions (Pham and Martin, 2009).

The fatigue strength exponent for the reinforced design was computed in relation to the fatigue strength parameter when succumb to aligned and nominal yawed flow conditions at mid and high rotational velocities. By means of the range comparison, illustrated in Fig. 21, the maximum fatigue strength exponent was acknowledged to occur at mid rotational velocities within nominal free-stream bearings.

Additionally, the material properties for the solid blade design was investigated, presented in Fig. 22. In comparison to the reinforced design, the temporal response lessened as the solid design portrayed higher rigidity. Similar to the reinforced design, the maximum fatigue strength exponent occurred at mid rotational velocities within nominal free-stream bearings. The material properties acknowledged for both designs were quasi-equivalent at mid and high rotational velocities. Despite establishing diminished forces upon the blades at the latter condition, the load cycle frequency was greater, hence contributing to the fatigue response.

In recognition of the temporal analyses, the variation in fatigue strength exponent, by considering the solid and reinforced internal blade designs through a 10 to 25-year design life within aligned and nominal flow bearings at mid and high rotational velocities, ranged from −0.24 to −0.46. In consideration that a fatigue strength exponent of −0.119 had been attained at a fatigue strength parameter of 557 MPa for a GFRP (Manjunatha et al., 2010), the modelled outcomes were acknowledged to fall within a rational arrangement.

5. Conclusion

This study put forward an investigation into the structural response of a ducted, high-solidity tidal turbine rotor in real flow conditions by means of a partitioned-approach numerical coupling between a blade-resolved, unsteady computational fluid dynamics solver and a finite-element solver. The research strived to overcome the limitations of prior analyses by acknowledging the explicit three-dimensional physicality of the rotor blades. By this means, static pressure and wall shear-stress parameters were imported from the hydrodynamic model and mapped along the blade surface of the structural model as loading boundary conditions. As a result, a coherent representation of the turbine rotor blade response in aligned and yawed free-stream flows was established.

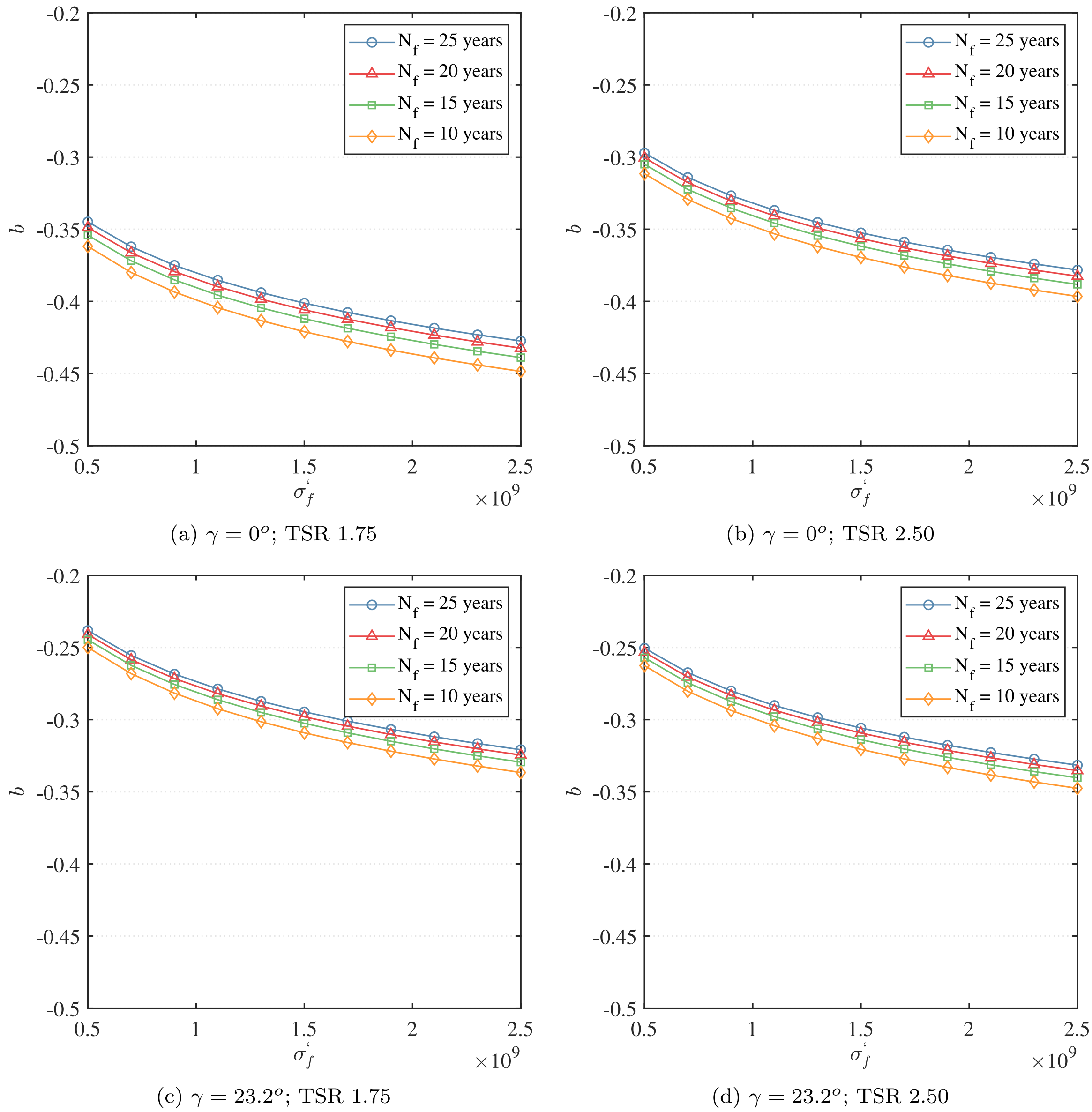

Fig. 21. Fatigue response of the reinforced high-solidity tidal turbine rotor blade design.

Three internal blade designs were put forward and analysed to acquire the more appropriate configuration for ducted, high-solidity rotor blades. In consideration of the structural outcomes derived, the geometrical characterisation of the three rotor designs was primarily acknowledged. The moment of inertia of the cored and reinforced blade were found to constitute 53.1% and 79.6% that of the solid blade, respectively. Subsequently, a hydrostatic analysis was undertaken to determine the structural integrity of the three blade designs at the installation water depth. All designs were acknowledged to sustain integrity, despite slight yielding apparent upon the cored design.

In continuation, a hydrodynamic analysis was undertaken. The highest normal strain response was induced by the cored blade design, portraying least rigidity, whereas the solid blade design attained the least response. The reinforced blade design provided an intermediate value. The investigated conditions were found to not exceed the ultimate strain value of the double-biased glass-fibre reinforced polymer for all blade designs. Due to the outcomes, the three designs were deemed to be largely equivalent in sustaining structural integrity at the operational conditions. Despite the outcomes, strain concentrations were induced at the leading edge of the blade, within the immediate vicinity of the root This occurred upon all three structural blade designs in all flow conditions. The concentrations resulted from the simultaneous bending and torsion responses.

Ancillary to the fracture analysis, a blade material cost analysis was undertaken to establish an estimation on the most cost-effective assortment of materials implementable for the three blade designs. The reinforced blade was acknowledged to require the least capital expenditure, whereas the solid blade required the highest.

In culmination, a fatigue analysis was undertaken to acknowledge an appropriate range of GFRP material properties for the designs within the considered flow conditions. By comparing the reinforced and solid blade designs, the values attained were found to be largely equivalent. Therefore, as a result of the outcomes attained and discussed, the reinforced internal blade design was considered to procure a favourable combination of high rigidity and comparatively lower weight, in addition to lower material capital expenditure. Albeit the outcome, further investigations are required to pursue a more appropriate design, specifically in establishing the optimised shell and webbing thickness for the operational conditions analysed, to further improve the performance of the ducted, high-solidity tidal turbine.

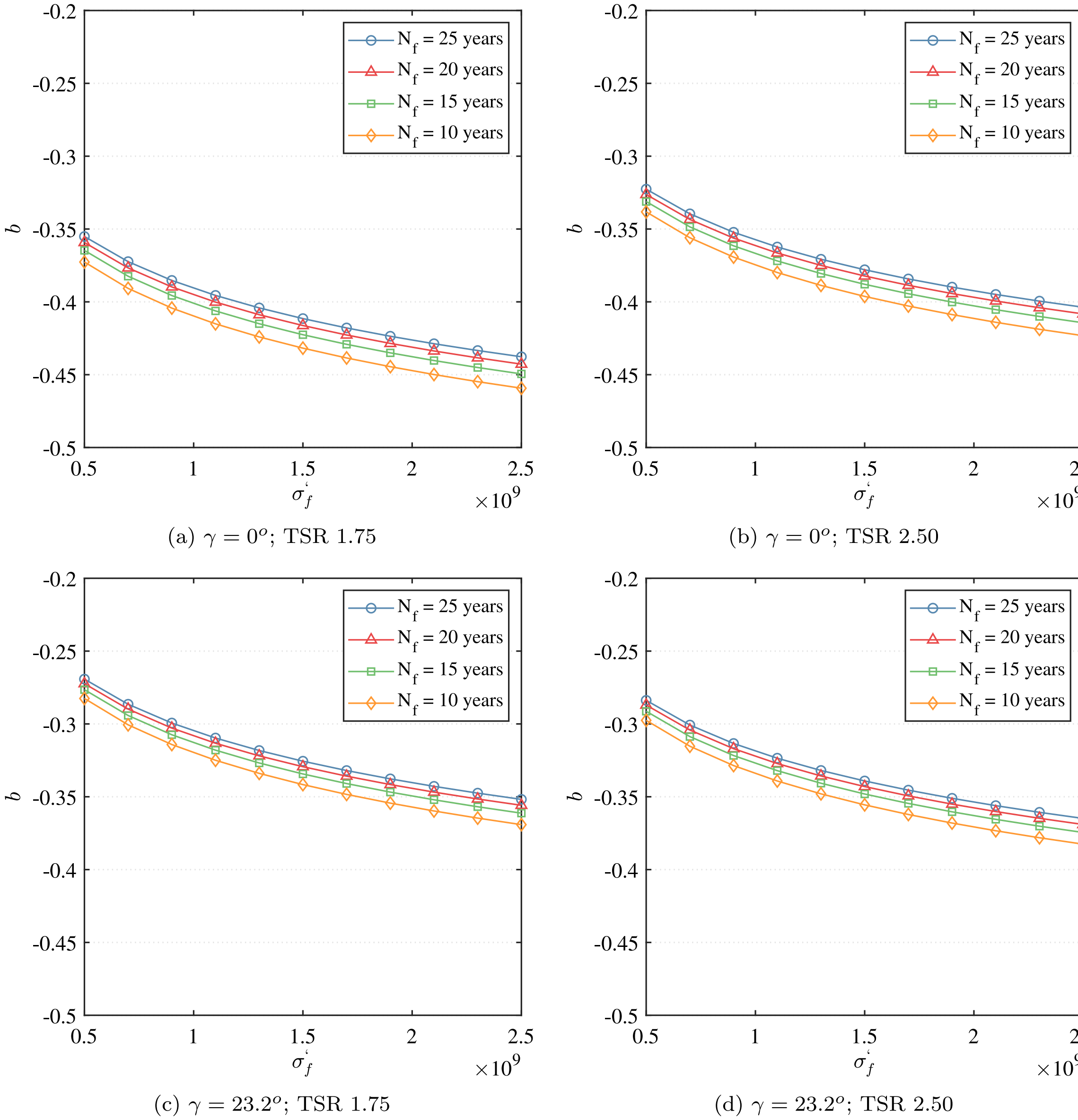

Fig. 22. Fatigue response of the solid high-solidity tidal turbine rotor blade design.

CRediT authorship contribution statement

Mitchell G. Borg: Conceptualization, Methodology, Software, Validation, Formal analysis, Investigation, Writing - original draft. **Qing Xiao:** Writing - review & editing, Supervision, Resources, Project administration. **Steven Allsop:** Conceptualization, Writing - review & editing, Resources, Formal analysis, Investigation. **Atilla Incecik:** Funding acquisition, Resources. **Christophe Peyrard:** Resources, Supervision.

Declaration of competing interest

The authors declare that they have no known competing financial interests or personal relationships that could have appeared to influence the work reported in this paper.

Acknowledgements

The research work disclosed in this publication is partially funded by the Endeavour Scholarship Scheme (Malta). Scholarships are part-financed by the European Union – European Social Fund (ESF) – Operational Programme II – Cohesion Policy 2014-2020: *"Investing in human capital to create more opportunities and promote the well-being of society"*, CCI number: 2014MT05SFOP001.

Results were obtained using ARCHIE-WeSt High Performance Computer (www.archie-west.ac.uk).

References

Allsop, S.C., 2018. Hydrodynamic Modelling for Structural Analysis of Tidal Stream Turbine Blades (Ph.D. thesis). University of Edinburgh, p. 285.

Allsop, S., Peyrard, C., Bousseau, P., Thies, P., 2018. Adapting conventional tools to analyse ducted and open centre tidal stream turbines. Int. Mar. Energy J. 1 (2), 91–99.

Allsop, S., Peyrard, C., Thies, P.R., Boulougouris, E., Harrison, G.P., 2017. Hydrodynamic analysis of a ducted, open centre tidal stream turbine using blade element momentum theory. Ocean Eng. 141, 531–542.

Barnes, R., Morozov, E., 2016. Structural optimisation of composite wind turbine blade structures with variations of internal geometry configuration. Compos. Struct. 152, 158–167.

Belloni, C., Willden, R., Houlsby, G., 2017. An investigation of ducted and open-centre tidal turbines employing CFD-embedded BEM. Renew. Energy 108, 622–634.

Betz, A., 1928. Windmills in the Light of Modern Research. Tech. Rep., National Advisory Committee for Aeronautics, Washington, DC, p. 29.

Bloomberg, L.P., 2020. OpenHydro Group Limited: Private Company Information - Bloomberg. https://www.bloomberg.com/profile/company/4074464Z:ID2018. (Accessed 24 December 2020).

Borg, M.G., Xiao, Q., Allsop, S., Incecik, A., Peyrard, C., 2020. A numerical performance analysis of a ducted, high-solidity tidal turbine. Renew. Energy 159, 663–682.

Borg, M.G., Xiao, Q., Allsop, S., Incecik, A., Peyrard, C., 2021. A numerical swallowing-capacity analysis of a vacant, cylindrical, bi-directional tidal turbine duct in aligned & yawed flow conditions. J. Mar. Sci. Eng. 9 (2).

Bortolotti, P., Berry, D., Murray, R., Gaertner, E., Jenne, D., Damiani, R., Barter, G., Dykes, K., 2019. A Detailed Wind Turbine Blade Cost Model. Tech. Rep. NREL/TP-5000-73585, National Renewable Energy Laboratory, Golden, Colorado, p. 69.

Boudounit, H., Tarfaoui, M., Saifaoui, D., Nachtane, M., 2020. Structural analysis of offshore wind turbine blades using finite element method. Wind Eng. 44 (2), 168–180.

Grogan, D., Leen, S., Kennedy, C., Bradaigh, C., 2013. Design of composite tidal turbine blades. Renew. Energy 57 (5), 151–162.

Kogan, A., Seginer, A., 1963. T.A.E. Rep. No. 32A: Final Report on Shroud Design. Tech. Rep., Department of Aeronautical Engineering, Technion – Israel Institute of Technology, Haifa, Israel.

Krstulovic-Opara, L., Klarin, B., Domazet, Z., 2009. A non-destructive wind turbine blade analysis based on the Thermal Stress Analysis. Split, Hrvatska.

Leong, M., Overgaard, L.C., Thomsen, O.T., Lund, E., Daniel, I.M., 2012. Investigation of failure mechanisms in GFRP sandwich structures with face sheet wrinkle defects used for wind turbine blades. Compos. Struct. 94 (2), 768–778.

Lilley, G.M., Rainbird, W.J., 1956. A Preliminary Report on the Design and Performance of Ducted Windmills. Tech. Rep. 102, College of Aeronautics, Cranfield, Bedfordshire, United Kingdom.

Luquet, R., Bellevre, D., Fréchou, D., Perdon, P., Guinard, P., 2013. Design and model testing of an optimized ducted marine current turbine. Int. J. Mar. Energy 2, 61–80.

Manjunatha, C., Taylor, A., Kinloch, A., Sprenger, S., 2010. The tensile fatigue behaviour of a silica nanoparticle-modified glass fibre reinforced epoxy composite. Compos. Sci. Technol. 70 (1), 193–199.

Nachtane, M., Tarfaoui, M., Saifaoui, D., Moumen, A.E., Hassoon, O., Benyahia, H., 2018. Evaluation of durability of composite materials applied to renewable marine energy: Case of ducted tidal turbine. Energy Rep. 4, 31–40.

O Rourke, F., Boyle, F., Reynolds, A., 2010. Tidal energy update 2009. Appl. Energy 87 (2), 398–409.

OpenHydro Group Ltd., 2017. Projects. http://www.openhydro.com/Projects. (Accessed 13 August 2017).

Pham, C.-T., Martin, V.A., 2009. Tidal current turbine demonstration farm in Paimpol-Brehat (Brittany): tidal characterisation and energy yield evaluation with Telemac. In: Proceedings of the 8th European Wave and Tidal Energy Conference, Uppsala, Sweden, vol. 710.

Rafiee, R., Tahani, M., Moradi, M., 2016. Simulation of aeroelastic behavior in a composite wind turbine blade. J. Wind Eng. Ind. Aerodyn. 151, 60–69.

Resistance Committee of the 28th ITTC., 2017. Uncertainty Analysis in CFD Verification and Validation, Methodology and Procedures. Technical Report, ITTC, Zürich, Switzerland.

Solvay, S.A., 2013. MTM 28 SERIES. https://www.solvay.com/en/product/mtm-28. (Accessed 22 November 2019).

The Canadian Press, 2018. Cape sharp tidal turbine in bay of fundy now being monitored remotely. https://www.cbc.ca/news/canada/nova-scotia/cape-sharp-tidal-turbine-remote-monitoring-environment-1.4814069. (Accessed 15 September 2018).

Wilcox, D.C., 2006. Turbulence Modeling for CFD, third ed. DCW Industries, Inc, San Diego, p. 515,

Zhang, J., Guo, L., Wu, H., Zhou, A., Hu, D., Ren, J., 2014. The influence of wind shear on vibration of geometrically nonlinear wind turbine blade under fluid–structure interaction. Ocean Eng. 84, 14–19.

Zhou, Z., Benbouzid, M., Charpentier, J.-F., Scuiller, F., Tang, T., 2017. Developments in large marine current turbine technologies – A review. Renew. Sustain. Energy Rev. 71, 852–858.

Zhu, J., Ni, X., Shen, X., 2019. Aerodynamic and structural optimization of wind turbine blade with static aeroelastic effects. Int. J. Low-Carbon Technol. 15 (1), 55–64.